Planar metal–insulator–metal diodes based on the Nb/Nb2O5/X material system

Matthew L. Chin, Prakash Periasamy, Terrance P. O'Regan, Matin Amani, Cheng Tan, Ryan P. O'Hayre, Joseph J. Berry, Richard M. Osgood III, Philip A. Parilla, David S. Ginley, and Madan Dubey

---

Articles you may be interested in

Conduction processes in metal–insulator–metal diodes with Ta2O5 and Nb2O5 insulators deposited by atomic layer deposition
J. Vac. Sci. Technol. A **32**, 01A122 (2014); 10.1116/1.4843555

Impact of electrode roughness on metal-insulator-metal tunnel diodes with atomic layer deposited Al2O3 tunnel barriers
J. Vac. Sci. Technol. A **30**, 01A113 (2012); 10.1116/1.3658380

Electrode effects on the conduction mechanisms in HfO 2 -based metal-insulator-metal capacitors
J. Appl. Phys. **106**, 064508 (2009); 10.1063/1.3226857

Experimental evidence for the role of electrodes and oxygen vacancies in voltage nonlinearities observed in high-k metal-insulator-metal capacitors
Appl. Phys. Lett. **91**, 172909 (2007); 10.1063/1.2803221

Controlled barrier modification in Nb/NbOx/Ag metal insulator metal tunnel diodes
J. Appl. Phys. **91**, 10134 (2002); 10.1063/1.1471385

Planar metal–insulator–metal diodes based on the Nb/Nb$_2$O$_5$/X material system

Matthew L. Chin[a),b)]
US Army Research Laboratory, Sensors and Electron Devices Directorate, 2800 Powder Mill Road, Adelphi, Maryland 20783

Prakash Periasamy[a),c)]
Department of Metallurgy and Materials Engineering, Colorado School of Mines, 1500 Illinois Street, Golden, Colorado 80401

Terrance P. O'Regan, Matin Amani, and Cheng Tan
US Army Research Laboratory, Sensors and Electron Devices Directorate, 2800 Powder Mill Road, Adelphi, Maryland 20783

Ryan P. O'Hayre
Department of Metallurgy and Materials Engineering, Colorado School of Mines, 1500 Illinois Street, Golden, Colorado 80401

Joseph J. Berry
National Renewable Energy Laboratory, 15013 Denver West Parkway, Golden, Colorado 80401

Richard M. Osgood III
US Army Natick Soldier Research, Development and Engineering Center, 15 Kansas Street, Natick, Massachusetts 01760

Philip A. Parilla and David S. Ginley
National Renewable Energy Laboratory, 15013 Denver West Parkway, Golden, Colorado 80401

Madan Dubey
US Army Research Laboratory, Sensors and Electron Devices Directorate, 2800 Powder Mill Road, Adelphi, Maryland 20783

The authors report the performance of various planar metal–insulator–metal (MIM) tunneling diodes, which are being investigated for use in rectenna devices for energy harvesting applications. Six cathode materials (M$_2$): Nb, Ag, Cu, Ni, Au, and Pt are studied in conjunction with Nb as the anode (M$_1$) and Nb$_2$O$_5$ (I) as the dielectric. The cathode materials selections were based on results from a prior rapid-screening study that employed a bent-wire metal cathode point-contact method. Planar devices, to enable analysis using standard MIM diode models, were fabricated with the resultant current density–voltage data obtained at both room temperature and 77 K. The tunnel barrier heights and dielectric properties for these systems were extracted from the modeling results. Nb/Nb$_2$O$_5$/Pt MIM diodes showed the best performance with an asymmetry ratio greater than 7700, a nonlinearity value of 4.7, and a responsivity of 16.9, all at 0.5 V and 300 K. These results confirm prior rapid-screening efforts and further validate the Nb/Nb$_2$O$_5$/Pt system in particular as a promising MIM architecture due to the low barrier height of the junction. © *2013 American Vacuum Society*. [http://dx.doi.org/10.1116/1.4818313]

I. INTRODUCTION

Rectenna devices, which operate via an optical antenna to absorb incident electromagnetic radiation and couple it to a rectifying element to generate a direct current (DC) voltage, have attracted interest for energy harvesting in the infrared (IR) and optical spectrums.[1–6] Typical components of a rectenna include an antenna structure that is optimized for absorption at a target wavelength, a rectifying diode to convert the incoming resonant current from the antenna to DC power for use by a load, a low-pass filter between the antenna and

rectifier to provide impedance matching and to prevent higher frequency harmonics generated by the rectifying diode from reradiating, and finally a DC filter between the rectifying diode and the load for coupling and impedance matching purposes. Rectenna systems are an intriguing alternative to photovoltaic (PV) solar-cell technologies since they are capable of converting a much wider spectral range into useable energy and due to their higher potential conversion efficiencies (reported to approach 84%).[3,5,7] It has been envisioned that with the right manufacturing processes, rectenna arrays could be fabricated onto flexible substrates and then integrated as an energy harvesting system into clothing, portable electronics, stationary infrastructure, and other mobile platforms.

However, several major technical hurdles must be overcome before this technology becomes a viable energy

---

[a)]M. L. Chin and P. Periasamy contributed equally to this work.
[b)]Electronic mail: matthew.l.chin2.civ@mail.mil
[c)]Present address: IBM Microelectronics, Mail Box 967A, 1000 River Street, Essex Junction, VT 05452; electronic mail: pperias@us.ibm.com

T$_{ABLE}$ I. List of cathode (M$_2$) work functions along with the work function difference between the cathodes and the Nb anode (M$_1$) as well as the difference between the cathodes and the electron affinity of the Nb$_2$O$_5$ oxide. The majority of the metal work functions was taken from literature (Refs. 1 and 26).

M$_2$	Metal work function (Φ_M) (eV)	Difference between M$_1$ (Nb) and M$_2$ Φ_M (eV)	Difference between Nb$_2$O$_5$ electron affinity and M$_2$ Φ_M (eV)
Nb	4.30[a]	0.00	0.40 (Ref. 1)
Ag	4.70[a]	0.40	0.80
Au	5.10 (Ref. 26)	0.80	1.20
Cu	4.65 (Ref. 26)	0.35	0.75
Pt	5.65 (Ref. 26)	1.35	1.75

[a]These values were directly measured by the authors using the Kelvin probe technique on a SKP SPVLE 450 (KP Technology).

solution for rugged and portable applications. The antenna must be optimized to address issues with polarization, bandwidth, efficiencies, and impedance matching with the diode. Rectennas fundamentally generate a lower voltage per antenna element than most traditional PV systems, and there are known issues with skin-effect resistance.[3] There are similar technical challenges for the rectifying diode, which needs to be designed to have a high asymmetry and high current density, while simultaneously having a very low turn-on voltage and RC time constant. Finally, in the overall system, fabrication challenges pose several issues for manufacturing. These components must be made on the nanoscale (to reduce the parasitic capacitance), necessitating the use of low throughput e-beam lithography processes. This paper focuses on some of the issues related to the rectifying diode element by studying metal–insulator–metal (MIM) diodes using the Nb/Nb$_2$O$_5$/M$_2$ material system, where M$_2$ represents a number of different top metals such as Nb, Ag, Cu, Ni, Au, and Pt studied independent from one another.

An MIM diode consists of bottom and top metal contacts (M$_1$ and M$_2$, respectively) separated by a very thin dielectric layer (I) and operates via the extremely fast (femtosecond) quantum-tunneling transport mechanism. MIM diodes have been reported with operating frequencies ranging from as high as 150 THz (Refs. 2, 6, 8, and 9) to the infrared,[4,10–13] as well as mm-wave radiation.[10] As a result, these systems are excellent candidates for the rectification of short and mid-wave infrared wavelengths. Additionally, MIM diodes show promise as a rectifying element for rectennas because their current density voltage (J–V) characteristics can have high nonlinearity and can support sufficiently high current densities.

It has been demonstrated previously that the MIM J–V response can be tuned from symmetric and linear to highly asymmetric and nonlinear based on the material stacks used.[1,14] In this study, a base Nb/Nb$_2$O$_5$ (M$_1$/I) material combination was selected as the foundation for the different top metals (M$_2$) since a high-quality Nb$_2$O$_5$ insulator can be grown reproducibly as a pinhole-free, uniform layer on top of the Nb using an anodic oxidation process under atmospheric conditions. The top metals (M$_2$): Nb, Ag, Cu, Ni, Au, and Pt were chosen based on findings from previous work by Periasamy *et al.*,[1] where these metals displayed symmetric (Nb) and asymmetric (Ag, Cu, Au, and Pt) J–V characteristics when used as the second metal layer in a MIM diode with Nb/Nb$_2$O$_5$. The latter four metals possess a relatively high work function difference with the Nb metal layer,

which is responsible for the high asymmetry, high nonlinearity, and increased probability of electron quantum tunneling through the insulator barrier.[1,2,4,5,15] Nevertheless, the previous study examined these metals in a point-contact architecture using metal wires as the top metals (M$_2$). This approach facilitated the screening of the candidate systems and established the proof-of-concept architecture selection but precluded quantitative modeling of the diodes.

Here, we demonstrate a set of MIM combinations based on the Nb/Nb$_2$O$_5$ system for the first time in a robust planar architecture fabricated via a photolithographic process. Work functions of the M$_2$ candidates used in this study range from 4.3 (Nb) to 5.65 eV (Pt), with the values shown in Table I. Hence, with respect to the M$_1$ anode (Nb), the M$_2$ candidates give a work function difference ($\Delta\varphi$) value ranging from ∼0 eV for the Nb/Nb$_2$O$_5$/Nb to 1.35 eV for the Nb/Nb$_2$O$_5$/Pt system. In Table I, the expected barrier heights for an ideal interface are shown in the last column. The resulting figures-of-merit achieved for several of these diode systems are among the highest reported in the literature. The measured J–V responses at both 300 and 77 K are qualitatively modeled based on the works of Simmons[16,17] to confirm the general responses seen in the experimental data and to analyze the current contributions from thermionic emission and quantum tunneling.

II. EXPERIMENT

The devices fabricated in this study were based on the Nb/Nb$_2$O$_5$ anode/dielectric combination with six different top contact metals: Ag, Cu, Ni, Au, and Pt (as well as Nb as a point of comparison). Niobium films with a typical thickness of 90–100 nm were deposited on silicon substrates using a DC magnetron sputtering system in a 0.67 Pa Ar plasma, after pumping down the chamber to a pressure of less than 1 mPa. These deposition conditions were optimized in order to minimize the average surface roughness of the metal films, which improves the yield and minimizes pinholes in the devices. The Nb$_2$O$_5$ insulator films were grown using an anodization process[1] in a 1 M H$_2$SO$_4$ electrolyte solution carried out at room temperature under potentiostatic control. This process is capable of creating a consistent, uniform oxide layer across the entire Nb film with a thickness variation limited to less than 1 nm. The thickness of the Nb$_2$O$_5$ thin films was typically 15 nm, which includes ∼3–5 nm of a native oxide, grown at the Nb interface in an ambient
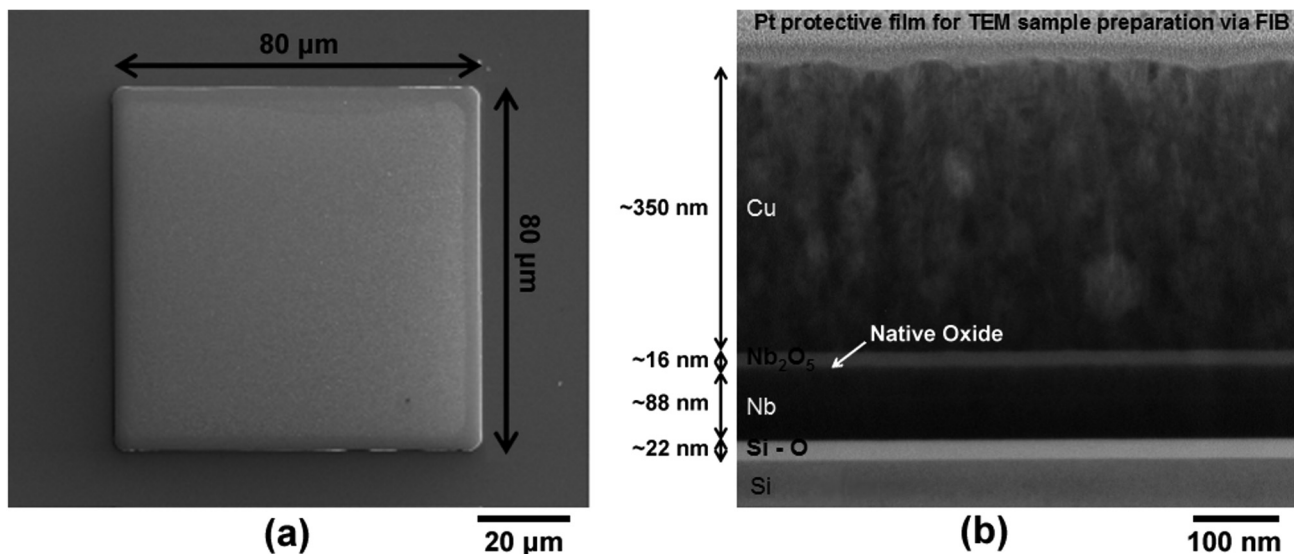
FIG. 1. (a) SEM image of a completed 80 μm by 80 μm Nb/Nb$_2$O$_5$/Cu diode after the lift-off procedure and (b) a TEM cross-sectional image showing the individual layers. Both the interfaces (Nb/Nb$_2$O$_5$) and (Nb$_2$O$_5$/Cu) are smooth and continuous, illustrating the quality of the deposited layers and the fabrication route. Based on previous work (Refs. [1], [14], and [18]), it is known that a native oxide forms at the Nb interface due to ambient air reacting with the exposed Nb surface.

environment. The morphology, thickness, and uniformity of the combined native oxide/anodically grown oxide layer were examined by cross-sectional transmission electron microscopy (XTEM) of several devices[14] with an example shown in Fig. [1]. In addition, an Nb/Nb$_2$O$_5$/Pt device with a 5 nm oxide was also fabricated in order to determine the effects of oxide thickness on the device performance.

The top contact metals were deposited and patterned using a lift-off procedure on the Si/Nb/Nb$_2$O$_5$ samples with electron-beam (Nb, Ag, Ni, Au, and Pt) or thermal (Cu) evaporation to create devices with a 6400 μm^2 active area. All top contact metal films were deposited with a base pressure of <0.2 mPa and a target thickness of 350–400 nm. The possibility of an intercalated interfacial oxide layer formed between the top metal and the Nb$_2$O$_5$ exists for some of the metals including Cu, Pt, and Ni, but the effect on the electrical characteristics of the MIM structures is probably small. Ultraviolet photoelectron spectroscopy (UPS) and x-ray photoelectron spectroscopy (XPS) measurements presented in one of the author's Ph.D. thesis revealed that amongst the top metals studied, only Cu and Pt showed slight evidence of a possible interaction with the Nb$_2$O$_5$ oxide.[18] The photolithographically fabricated MIM diodes were measured under vacuum (<0.3 mPa) at both 300 and 77 K using a Keithley 4200 semiconductor characterization system. This experimental system permitted J–V responses in our devices to be measured to as low as 1×10^{-10} A/cm^2. Contact to the bottom metal was made by mechanically removing the blanket layer of Nb$_2$O$_5$.

III. RESULTS AND DISCUSSION

A. Metrology

Several recent studies[19,20] have shown that electrode surface roughness plays a critical role in the performance of MIM devices, since for many crystalline metal films, the surface roughness is on the order of the dielectric thickness. This can lead to localized regions with very high conductance and pinhole defects in the insulator, as well as very poor device reproducibility and yield. Therefore, the deposition conditions for the Nb films used for this study were optimized to minimize the electrode surface roughness. Through atomic force microscopy (AFM), it was found that Nb films with an average surface roughness of 2 nm could be obtained for a film thickness of 90–100 nm using lower sputtering powers and pressures. An AFM image of one such electrode is shown in Fig. [2]. XTEM images of a typical device are shown in Fig. [1], confirming the bottom electrode thickness ($\sim$90 nm) and depicting the presence of the anodic oxidized film, with a thickness of approximately 16 nm. While it is
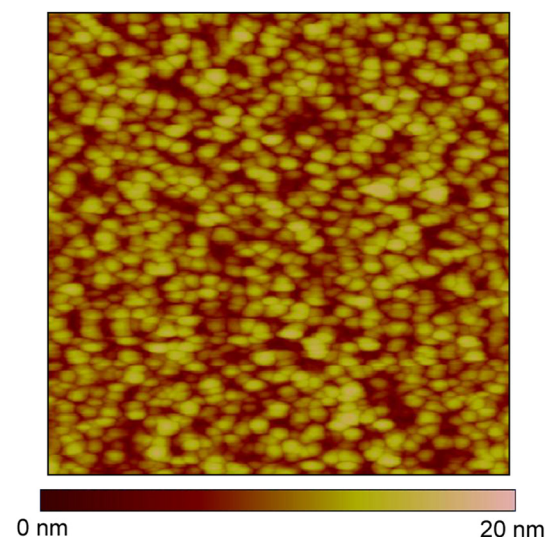

FIG. 2. (Color online) AFM image of a typical sputtered Nb film showing a RMS surface roughness of 1.5 nm for a film thickness of 90–100 nm over a 1 μm $\times$ 1 μm scan area.

difficult to distinguish in Fig. 1, in previous published work, we have determined that a thin ($\sim$3–5 nm) native oxide is present at the interface between the niobium and the anodically grown niobium oxide.[14] Both the native oxide and the anodically grown oxide are amorphous and possess an oxygen/niobium ratio consistent with Nb$_2$O$_5$.[14] The thickness and uniformity of the oxide grown over the Nb was verified across the samples using spectroscopic ellipsometry and x-ray reflectivity (XRR). These measurements were consistent with the oxide thickness values obtained from XTEM (within $\pm$2 nm) and indicated a surface roughness parameter of $\sim$2 nm, consistent with the AFM results.

B. Electrical characterization

Asymmetry (f_{ASYM}), nonlinearity (f_{NL}), and responsivity (f_{RES}) are typically used as the figures-of-merit for diodes in a number of applications including as a rectifier in rectenna devices.[1,2,6,15,19,21,22] The asymmetry, f_{ASYM}, is defined as

$$f_{ASYM} = \left| \frac{J_F}{J_R} \right|, \tag{1}$$

where J_F is defined as the current density through the diode when swept with a positive, forward bias and where J_R is defined as the current density through the diode when swept with a negative, reverse bias. The ratio helps determine at which applied voltage to operate the device so that rectification can occur. Typically targeted f_{ASYM} values for diodes should be much greater than 1. A value of 1 indicates a symmetric but not necessarily linear device. The nonlinearity, f_{NL}, is defined as

$$f_{NL} = \frac{dJ}{dV} \bigg/ \frac{J}{V}, \tag{2}$$

where J is the diode current density and V is the applied potential across the diode. Ideally, the MIM diode should also show a high nonlinearity, on the order of 3 or greater.[4] The f_{NL} in MIM tunnel diodes is ideally dominated by the quantum tunneling mechanism, which has dynamics that occur at the femtosecond timescale to produce the high-speed transport and conduction required for rectennas to operate at optical frequencies.[1] The responsivity, f_{RES}, is defined as

$$f_{RES} = \frac{d^2J}{dV^2} \bigg/ \frac{dJ}{dV}, \tag{3}$$

where J is the diode current density and V is the applied potential across the diode. The responsivity is the ratio between the rectified current and the time varying power coupled into the junction, as determined by the local value of the second derivative of the junction's J–V characteristic at the operating point. Typically, values greater than 7 V^{-1} are desirable.[1,4]

Since the devices fabricated in this study possess relatively thick Nb$_2$O$_5$ oxide films, typically with oxide thickness (s) values averaging around 12–18 nm, thermionic emission might be expected as the dominant mode of

transport.[16] As described in the modeling, the quantum tunneling mechanism of carrier transport only contributes significantly at oxide thicknesses of 5 nm or less. However, it should be noted that it is the effective oxide barrier thickness (Δs) that is important in the model rather than the physical insulator thickness, so that current contributions due to tunneling can be significant even at s > 5 nm. The discrepancy between Δs and s results from the fact that under biased conditions and/or in appropriate M$_1$IM$_2$ structures with very dissimilar work functions of the two metals, the effective oxide barrier can be very small, allowing for Fowler–Nordheim tunneling to take place. The measured J–V responses of typical Nb/Nb$_2$O$_5$/Pt diodes with both s = 5 and s = 15-nm-thick insulator layers are shown in Figs. 3(a) and 3(b) at 300 and 77 K. The data indicate a seven order-of-magnitude improvement in the current density at cryogenic temperature where the tunneling currents dominate in contrast to the modest increase in current density at room temperature. Moreover, the key figures-of-merit of the 15 nm insulator device is significantly improved compared to the 5 nm device, likely due to the reduced impact of defects in the oxide layer.

A comparison of the J–V response for the 15 nm Nb$_2$O$_5$ insulator devices with different M$_2$ is shown in Fig. 4 at both 300 and 77 K. Sixteen devices from each of the six different M$_2$ metals were characterized. The results shown in Fig. 4 and the subsequent figures show a representative device. Variation in the current density between devices with the same M$_2$ metal ranged $\pm$7%. The device models discussed in Sec. IV were fit to these data and used to extract the barrier heights for the various cathode materials. We estimated that the Nb/Nb$_2$O$_5$ interface possesses a barrier height of only 0.4 eV, which is relatively low, making it a good material system for this application. Regardless of the cathode material, all systems show a similar reduction in conduction at 77 K compared to the data taken at 300 K. The asymmetry, nonlinearity, and responsivity of the various systems are plotted in Figs. 5–7 based on the J–V data recorded at 300 K. Due to the significantly reduced current densities, the figure-of-merits could not be accurately calculated at cryogenic temperatures for the 15 nm devices. However, we were able to calculate these figures-of-merit for the Nb/Nb$_2$O$_5$/Pt device with a 5 nm thick insulator layer. Figures-of-merit were calculated at 0.5 V and are listed in Table II.

The asymmetries at 0.5 V for each of the devices in this study versus the work function of the top electrode are shown in Fig. 8. The resulting correlation strongly supports the relationship between the forward/reverse J–V characteristics (asymmetry figure-of-merit) and metal work function differences based on thermionic emission, as described by Simmons.[16] Equation (4) is the fitted equation to the plot shown in Fig. 8, relating the asymmetry with the work function difference between the bottom (M$_1$) and top metal (M$_2$) of the MIM diode

$$f_{ASYM} = 10^{3.3137(\varphi_{M2} - \varphi_{M1})}, \tag{4}$$

where φ_{M2} is the work function of the top metal (M$_2$) and φ_{M1} is the work function of the bottom metal (M$_1$, and in
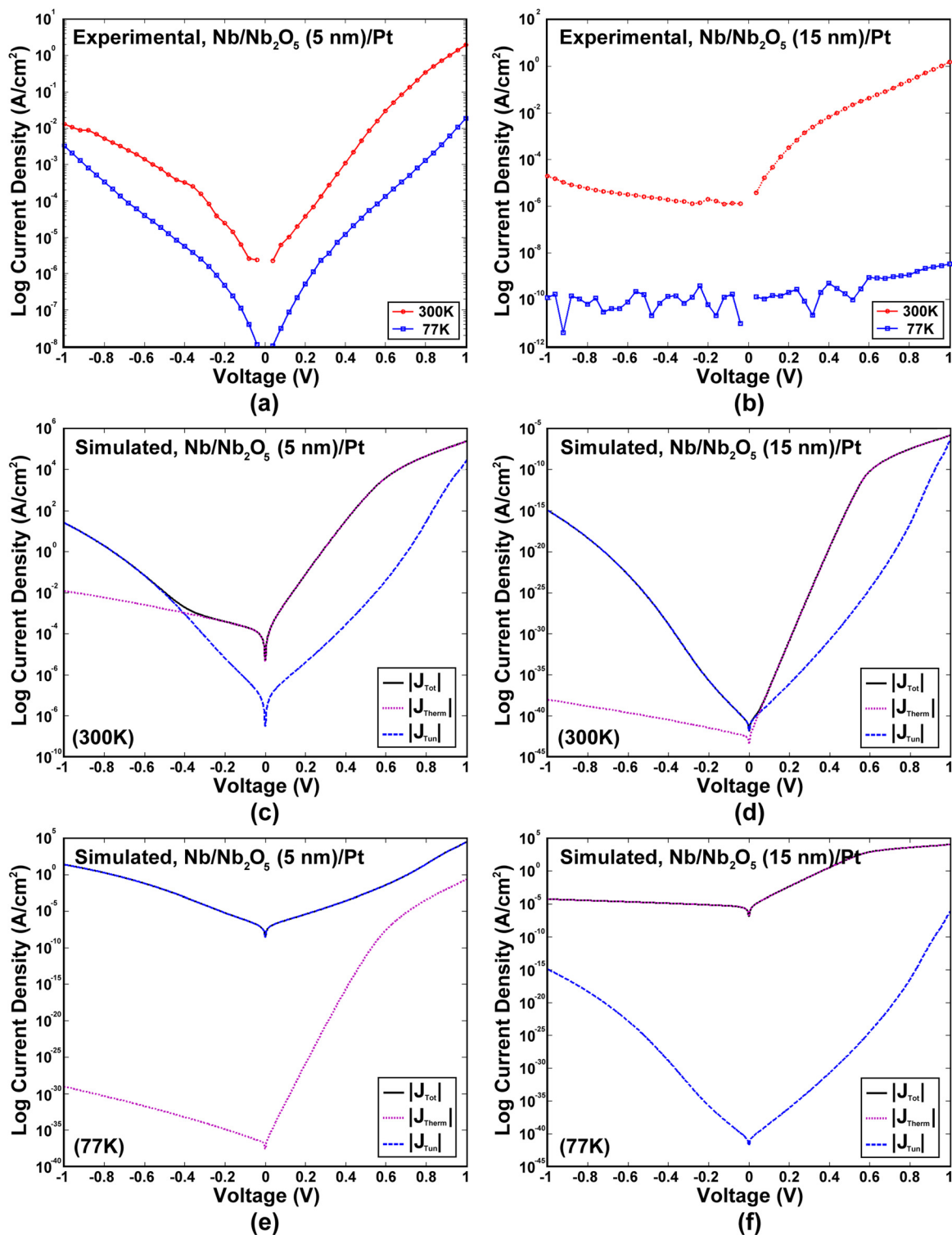
FIG. 3. (Color online) Experimental and simulated plots of current density vs the voltage are shown for Nb/Nb$_2$O$_5$/Pt MIM diodes. Represented in (a) and (b) is experimental J–V characteristics for an $80\,\mu m \times 80\,\mu m$ device with a 5 and 15-nm-thick Nb$_2$O$_5$ insulator layer taken at 300 and 77 K, respectively. Represented in (c) and (d) are the modeled J–V characteristics for a device with a 5 and 15-nm-thick Nb$_2$O$_5$ insulator layer taken at 300 K, respectively. Represented in (e) and (f) are the modeled J–V characteristics for a device with a 5 and 15-nm-thick Nb$_2$O$_5$ insulator layer taken at 77 K, respectively.

all cases for this study, is Nb). It is clear that the Nb/Nb$_2$O$_5$/Pt material system offers the best performance for rectenna applications. With an asymmetry ratio greater than 74 000 at 1 V and greater than 7700 at 0.5 V, a nonlinearity value of greater than 4.7 at 0.5 V, and a responsivity of more than 280 at 0.5 V, the values reported here are greater

than for any previously reported MIM device at the same bias voltage. The voltage at which the forward current is an order of magnitude greater than at the mirrored negative voltage was 80 mV, which is in a voltage range that is compatible with what an optical antenna would be expected to generate.
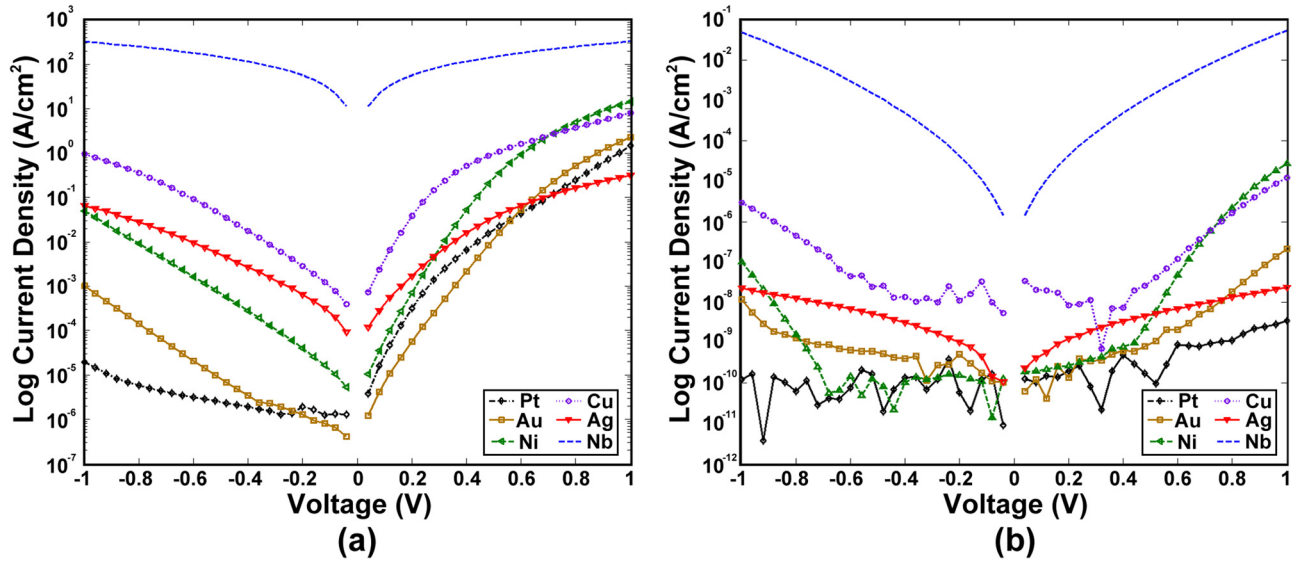
FIG. 4. (Color online) Current density vs applied voltage is plotted for planar Nb/Nb$_2$O$_5$-based MIM diodes with varying cathode materials and a 15 nm thick dielectric layer at 300 K (a) and 77 K (b). The cathode metals measured include Pt, Au, Ni, Cu, Ag, and Nb.

IV. MODELING

The devices in this study were modeled by combining standard models for thermionic emission and tunneling, including the image potential correction to the electrostatic potential in the dielectric layer. The thermionic emission-limited current density over the barrier is given by[16]

$$J = A_{th}T^2 e^{-\varphi/k_B T}(1 - e^{-qV/k_B T}) \qquad (5)$$

in which φ is the maximum barrier height, T is the absolute temperature, and

$$A_{th} = 4\pi q m_0 k_B^2/h^3, \qquad (6)$$

where m_0 is the electron mass, k_B is Boltzmann's constant, h is Plank's constant, q is the electron charge, and V is the applied bias. The tunneling-limited current density through a MIM diode is given by[17]

$$J = J_0\left\{ \bar{\varphi}e^{-A_{tun}\bar{\varphi}^{\frac{1}{2}}} - (\bar{\varphi} + qV)e^{-A_{tun}(\bar{\varphi}+qV)^{\frac{1}{2}}} \right\}, \qquad (7)$$

where $J_0 = q/2\pi h(\beta\Delta s)^2$, β is a dimensionless correction factor (β is set to unity in this work), Δs is the effective tunneling distance after including the image potential, and $\bar{\varphi}$ is the mean barrier height above the Fermi level of the negatively biased electrode.[16,17] The factor in the exponent is $A_{tun} = (2m)^{\frac{1}{2}}(4\pi\beta\Delta s/h)$.[17] With the thermal and tunneling limited currents defined, the total current density is
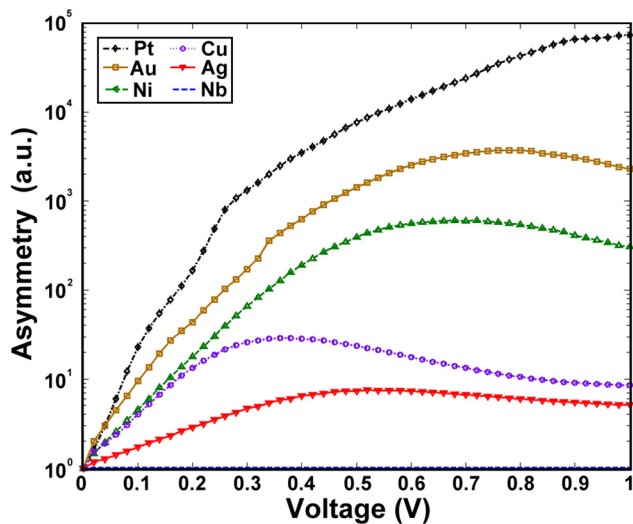

FIG. 5. (Color online) Asymmetry is plotted by taking the difference between absolute value of the ratio between the forward and reverse current for a given voltage value. The asymmetry was taken from planar 80 μm × 80 μm Nb/Nb$_2$O$_5$-based MIM diodes with a 15 nm thick Nb$_2$O$_5$ layer measured at 300 K.
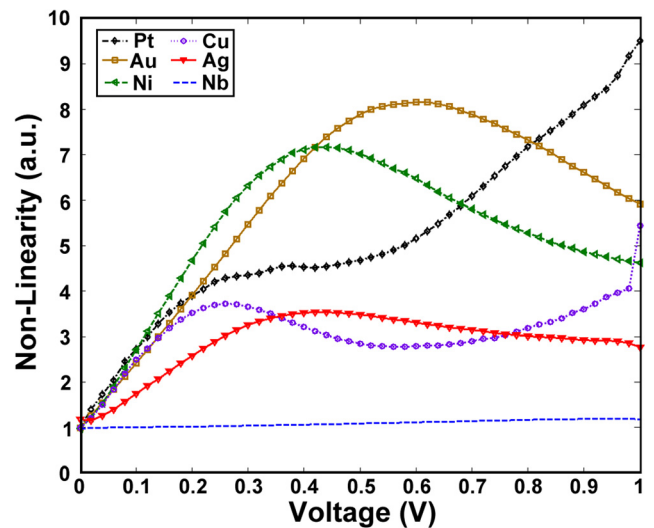

FIG. 6. (Color online) Nonlinearity is plotted by taking the instantaneous slope of the current–voltage ratio at a particular applied voltage and dividing by current–voltage ratio at that same applied voltage. The nonlinearity was taken from planar 80 μm × 80 μm Nb/Nb$_2$O$_5$-based MIM diodes with a 15 nm thick Nb$_2$O$_5$ layer measured at 300 K.
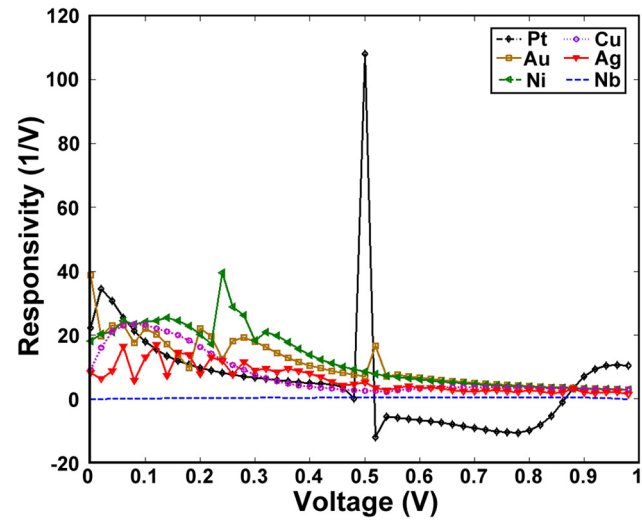
FIG. 7. (Color online) Responsivity is plotted by taking the derivative of the instantaneous slope of the current–voltage ratio at a particular applied voltage and dividing by the instantaneous slope of the current–voltage ratio at that same applied voltage. The responsivity was taken from planar 80 μm × 80 μm Nb/Nb$_2$O$_5$-based MIM diodes with a 15 nm thick Nb$_2$O$_5$ layer measured at 300 K.

$$J_{total} = J_{therm} + J_{tunnel}. \qquad (8)$$

In order to accurately model the thermionic-emission and tunneling limited current in these devices, we find a constant barrier height set by $\varphi = \Phi_m - \chi_{ins}$, where Φ_m is the metal work function and χ_{ins} is the insulator electron affinity, could not effectively describe the data. In order to address this, the image potential between the two electrodes was approximated,[16,17] providing us an expression for the total potential energy as a function of applied bias

$$V_{tot} = \varphi_1 + (\Delta\Phi - qV)\left(\frac{x}{s}\right) + \frac{-0.288s}{Kx(s-x)}, \qquad (9)$$

where φ_1 is the barrier height of the grounded electrode, K is the high-frequency relative dielectric constant, s is the physical insulator thickness, x is the position coordinate perpendicular to the layers in the MIM diode structure, and $\Delta\Phi$ is the difference in work function of the metal electrodes. This correction results in a reduction in the barrier height by nearly 0.2 eV at an external bias of 1 V.

The procedure begins by adjusting K and the Nb/Nb$_2$O$_5$ barrier height to find a best fit for the symmetric Nb/Nb$_2$O$_5$ (15 nm)/Nb diode at 300 K. For all subsequent fitting, the K value and Nb/Nb$_2$O$_5$ (M$_1$/I) barrier height are fixed, leaving only the Nb$_2$O$_5$/cathode metal (I/M$_2$) as the remaining adjustable parameter. The K value used here is 4, a best-guess parameter similar to many oxides as there is little experimental data in the literature, and the extracted barrier heights are listed in Table II. It is important to note here that the extracted barrier heights follow the correct trends, but should not be taken as quantitative constants as we have approximated $\beta = 1$ and have not considered other conduction mechanisms such as Pool–Frenkel emission.[23] Figures 3(c) and 3(d) show the modeled total [Eq. (8)], thermionic-limited [Eq. (5)], and tunneling-limited [Eq. (7)] current as well as its components for a 5 and 15 nm Nb$_2$O$_5$ insulator, respectively at 300 K, including the image potential correction. Figures 3(e) and 3(f) show the modeled currents for a 5 and 15-nm-thick Nb$_2$O$_5$ insulator, respectively at 77 K. The image potential correction is included in these figures as well. The barrier heights used in the model are 0.275 eV (Nb/Nb$_2$O$_5$) and 0.85 eV (Pt/Nb$_2$O$_5$) with K = 4. Figure 3 illustrates that while the model does not capture the quantitative current–voltage data, it helps us understand the qualitative aspects, showing the dominant conduction mechanisms in the different voltage and temperature regimes. For instance, for the 15-nm-thick insulator, the model reveals that the experimental data are dominated by thermionic emission at 300 K, while at 77 K all currents are below the noise floor, except for a hint of tunneling current at larger positive voltages. On the other hand, for the 5 nm thick insulator, comparing the experimental and modeling data suggest the current is tunneling dominated at 77 K, while at 300 K, there may be a mix of tunneling and thermionic currents. There are number of important reasons that the model fails to completely capture the quantitative aspects of the experimental data. First, the model is one-dimensional while the actual device will have variations in two-dimensions (insulator thickness, work function/barrier height, dielectric constant, etc.) that are not accounted for in the model. Second, there may be other transport mechanisms that the model does not consider, such as trap assisted tunneling and oxygen migration/filament forming current paths.[24,25] While a more quantitative model would be advantageous, the simplicity of the model we used is

TABLE II. Summary of the figure-of-merits calculated at 0.5 V forward bias and modeled barrier height for Nb/Nb$_2$O$_5$-based MIM diodes with different M$_2$ candidates reported in this study. The highest figure-of-merits reported in the literature at 0.5 V is also provided for comparison (Ref. 1).

| Material system	Asymmetry	Nonlinearity	Responsivity (1/V)	M$_2$ barrier height used in model (eV)
Nb/Nb$_2$O$_5$ (15 nm)/Nb (300 K)	1.0	1.1	0.4	0.275
Nb/Nb$_2$O$_5$ (15 nm)/Ag (300 K)	7.4	3.5	5.0	0.65
Nb/Nb$_2$O$_5$ (15 nm)/Cu (300 K)	22.2	2.8	6.4	0.7
Nb/Nb$_2$O$_5$ (15 nm)/Ni (300 K)	396.5	7.1	8.5	0.7
Nb/Nb$_2$O$_5$ (15 nm)/Au (300 K)	1430.8	8.0	7.0	0.75
Nb/Nb$_2$O$_5$ (15 nm)/Pt (300 K)	7742.0	4.7	52.2	0.85
Nb/Nb$_2$O$_5$ (5 nm)/Pt (300 K)	9.8	8.2	16.9	—
Nb/Nb$_2$O$_5$ (5 nm)/Pt (77 K)	2.7	5.5	5.4	—
Nb/Nb$_2$O$_5$ (15 nm)/Pt (300 K) (Ref. 1)	1500	20	0.5	—
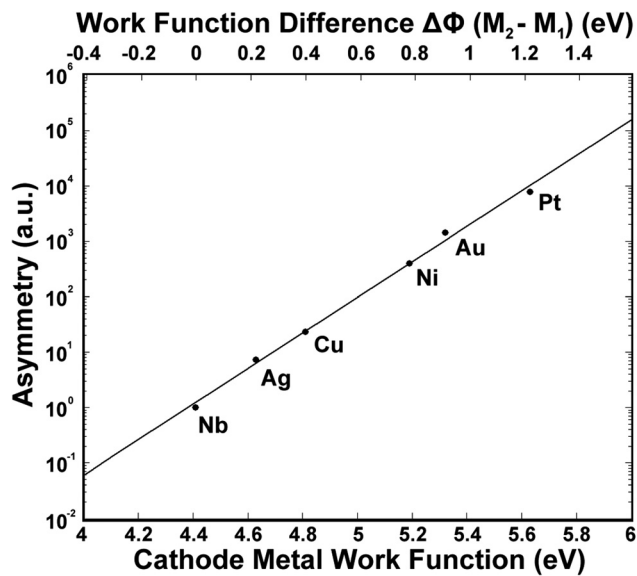
FIG. 8. Asymmetry measured at a 0.5 V bias (and 300 K) is plotted as a function of the cathode metal work function and the work function difference between M$_1$ and M$_2$. A positive exponential increase in asymmetry is shown with increasing cathode work function. The fitted trend line of this plot is shown as Eq. (4).

informative with respect to the major trends in barrier heights and determining the strength of thermionic emission versus tunneling dominated transport.

V. SUMMARY AND CONCLUSIONS

In summary, planar MIM diodes based on Nb/Nb$_2$O$_5$ blanket films with six different top electrode metals were fabricated and characterized. The top metals reviewed were Ag, Au, Cu, Ni, Nb, and Pt. Characterization of the MIM diodes J–V characteristics were performed at both 300 and 77 K. It was found that the material systems with Au, Ag, Cu, Nb, and Pt top electrodes possessed asymmetric properties with the highest performing devices in each of those material systems surpassing the minimum desired figure-of-merit asymmetry and nonlinearity. In general, the measurements taken at 77 K had current densities typically 10^4–10^8 lower than the measurements taken on the same devices at 300 K, indicating that thermionic emission is the dominant mechanism of conduction in all devices at room temperature. Additionally, the measurements taken at 77 K possessed substantially lower asymmetry and nonlinearity values. Among the 300 K measurements, the Nb/Nb$_2$O$_5$/Pt material system possessed the most desirable performance values and characteristics for use as a potential rectifier. With record figure-of-merit values based on the J–V characteristics, this material system possesses great promise for future integration into a rectenna system.

[1]P. Periasamy, J. J. Berry, A. A. Dameron, J. D. Bergeson, D. S. Ginley, R. P. O'Hayre, and P. A. Parilla, Adv. Mater. **23**, 3080 (2011).

[2]S. Krishnan, H. L. Rosa, E. Stefanakos, S. Bhansali, and K. Buckle, Sens. Actuators, A **142**, 40 (2008).

[3]M. Sarehraz, K. Buckle, T. Weller, E. Stefanakos, S. Bhansali, Y. Goswami, and S. Krishnan, *Conference Record of the 31st IEEE Photovoltaic Specialists Conference 2005* (IEEE, Lake Buena Vista, FL, 2005), pp. 78–81.

[4]B. Berland, *Photovoltaic Technologies Beyond the Horizon: Optical Rectenna Solar Cell* (NREL, Golden, CO, 2011), p. 16.

[5]D. K. Kotter, S. D. Novack, W. D. Slafer, and P. Pinhero, *ASME 2008 2nd International Conference on Energy Sustainability* (ASME, Jacksonville, FL, 2008), Vol. 2, pp. 409–415.

[6]S. Grover and G. Moddel, IEEE J. Photovoltaics **1**, 78 (2011).

[7]W. C. Brown, IEEE Trans. Microwave Theory Tech. **32**, 1230 (1984).

[8]M. Nagae, Jpn. J. Appl. Phys., Part 1 **11**, 1611 (1972).

[9]D. A. Jennings, F. R. Petersen, and K. M. Evenson, Appl. Phys. Lett. **26**, 510 (1975).

[10]T. K. Gustafson, R. V. Schmidt, and J. R. Perucca, Appl. Phys. Lett. **24**, 620 (1974).

[11]G. M. Elchinger, A. Sanchez, J. Davis, and A. Javan, J. Appl. Phys. **47**, 591 (1976).

[12]S. Faris, T. Gustafson, and J. Wiesner, IEEE J. Quantum Electron. **9**, 737 (1973).

[13]S. Y. Wang, S. M. Faris, D. P. Siu, R. K. Jain, and T. K. Gustafson, Appl. Phys. Lett. **25**, 493 (1974).

[14]P. Periasamy, H. L. Guthrey, A. I. Abdulagatov, P. F. Ndione, J. J. Berry, D. S. Ginley, S. M. George, P. A. Parilla, and R .P. O'Hayre, Adv. Mater. **25**, 1301 (2013).

[15]J.-J. Huang, C.-W. Kuo, W.-C. Chang, and T.-H. Hou, Appl. Phys. Lett. **96**, 262901 (2010).

[16]J. G. Simmons, J. Appl. Phys. **35**, 2472 (1964).

[17]J. G. Simmons, J. Appl. Phys. **34**, 1793 (1963).

[18]P. Periasamy, "Metal-insulator-metal diodes for THz and optical energy harvesting: Development of materials design principles," Doctoral dissertation (Colorado School of Mines, 2013).

[19]E. W. Cowel III, N. Alimardani, C. C. Knutson, J. F. Conley, Jr., D. A. Keszler, B. J. Gibbons, and J. F. Wager, Adv. Mater. **23**, 74 (2011).

[20]N. Alimardani, E. W. Cowell III, J. F. Wager, J. Conley, D. R. Evans, M. Chin, S. J. Kilpatrick, and M. Dubey, J. Vac. Sci. Technol. A **30**, 01A113 (2012).

[21]K. Choi, G. Ryu, F. Yesilkoy, A. Chryssis, N. Goldsman, M. Dagenais, and M. Peckerar, J. Vac. Sci. Technol. B **28**, C6O50 (2010).

[22]Kwangsik Choi, M. Dagenais, and M. M. Peckerar, *Semiconductor Device Research Symposium, ISDRS '09* (IEEE, College Park, MD, 2009), p. 1.

[23]J. G. Simmons, Phys. Rev. **155**, 657 (1967).

[24]M. Villafuerte, G. Juarez, S. P. de Heluani, and D. Comedi, Physica B **398**, 321 (2007).

[25]V. K. Yarmarkin, S. G. Shul'man, and V. V. Lemanov, Phys. Solid State **50**, 1841 (2008).

[26]H. B. Michaelson, J. Appl. Phys. **48**, 4729 (1977).